

JGR Space Physics

RESEARCH ARTICLE

10.1029/2023JA031787

Key Points:

- We report the first direct observation of the rising-tone chorus triggered by the enhanced solar wind pressure with Van Allen Probes
- Rising tones are triggered from the preexisting whistlers by the first increase of solar wind pressure, and then intensified by the second rise
- The reduced inhomogeneity of geomagnetic fields caused by the enhanced solar wind pressure is the major factor to control the nonlinear evolution

Correspondence to:

X. Gao and R. Chen,
gaoxl@ustc.edu.cn;
rchen@mail.ustc.edu.cn

Citation:

Zhou, X., Gao, X., Chen, R., Lu, Q., Ke, Y., Ma, J., & Kong, Z. (2023). Direct observation of rising-tone chorus triggered by enhanced solar wind pressure. *Journal of Geophysical Research: Space Physics*, 128, e2023JA031787. <https://doi.org/10.1029/2023JA031787>

Received 16 JUN 2023
Accepted 16 OCT 2023

Direct Observation of Rising-Tone Chorus Triggered by Enhanced Solar Wind Pressure

Xuan Zhou^{1,2,3} , Xinliang Gao^{1,2,3,4} , Rui Chen^{1,2,3} , Quanming Lu^{1,2,3,4} , Yangguang Ke^{1,2,3,4} , Jiuqi Ma^{1,2,3} , and Zhenyu Kong^{1,2,3} 

¹Deep Space Exploration Laboratory, School of Earth and Space Sciences, University of Science and Technology of China, Hefei, China, ²CAS Key Laboratory of Geoscience Environment, Hefei, China, ³CAS Center for Excellence in Comparative Planetology, Hefei, China, ⁴Collaborative Innovation Center of Astronautical Science and Technology, Harbin, China

Abstract Chorus waves play a significant role in both electron precipitation and acceleration in Earth's radiation belts. Their generation includes the initial linear process and subsequent nonlinear process. After the amplitude of whistler-mode waves reaches a sufficient value in the linear phase, the nonlinear process takes effect and results in the frequency chirping of chorus waves. Here we present the first report on the generation and intensification of rising-tone chorus driven by two sudden increases of solar wind dynamic pressure observed by Van Allen Probes on 20 December 2015. First, whistler-mode waves are excited by the anisotropic thermal electrons (~ 10 s keV), which is quite consistent with the linear theoretical expectation. Then, rising-tone chorus waves are nonlinearly generated from the existing whistler-mode waves, triggered by the first increase of solar wind dynamic pressure. Subsequently, the second increase of solar wind pressure further intensifies the rising-tone chorus. Based on the nonlinear theoretical model and Ts04 magnetic field model, we demonstrate that the decreasing inhomogeneity of the background magnetic field due to the increasing solar wind dynamic pressure is the major cause to trigger rising tones, which essentially reduces the wave amplitude threshold of the nonlinear process. Our study emphasizes the significance of solar wind dynamic pressure in the Earth's radiation belts from a micro perspective.

1. Introduction

Chorus waves are right-handed polarized electromagnetic emissions widely observed inside the plasma trough (Burtis & Helliwell, 1969). Satellite observations reveal that chorus waves typically exhibit hiss-like emissions, rising or falling tones in the frequency range of $0.1\text{--}0.5f_{ce}$ (lower band) and $0.5\text{--}0.8f_{ce}$ (upper band; f_{ce} denotes the equatorial electron gyrofrequency) (Gao et al., 2014, 2019; Gurnett et al., 2001; Santolík, Parrot, & Lefeuvre, 2003; Santolík, Gurnett, et al., 2003). They can not only precipitate $\sim 0.1\text{--}30$ keV electrons into the upper atmosphere but also accelerate hundreds of keV electrons to relativistic energies, thus exerting strong influences on electron dynamics of Earth's radiation belts (Horne et al., 2003; Mourenas et al., 2014; Ni et al., 2008). Previous theoretical and simulation studies have suggested that the generation of chorus waves can be regarded as the combination of linear and nonlinear processes. Initially, whistler mode waves are excited at the equator by several to tens of keV anisotropic electrons from thermal noises via the linear process (Horne et al., 2005; Kennel, 1966; Li et al., 2009, 2016). When the wave amplitude reaches the threshold amplitude and the wave optimum amplitude is greater than the threshold amplitude, the nonlinear effect is triggered to cause the frequency chirping of chorus waves (Omura, 2021; Omura et al., 2008; Omura & Nunn, 2011). Furthermore, the repetitive frequency chirping of chorus waves are mediated by the azimuthal drift of energetic electrons (Gao et al., 2022; Lu et al., 2021). Several parameters, including the ratio of hot and cold electrons, the anisotropy of resonance electrons, and the intensity and inhomogeneity of the background magnetic field, together determine the nonlinear growth of chorus waves, and most of them are strongly dependent on solar wind conditions.

With the arrival of interplanetary shock, a rapid increase in solar wind dynamic pressure causes the compression of the dayside magnetosphere. On the one hand, it may cause the betatron acceleration of electrons by the abrupt enhancement of magnetic field intensity, and therefore the electrons have a higher anisotropy (Tang et al., 2009). On the other hand, the inhomogeneity of background magnetic field may be reduced, and therefore result in a smaller threshold amplitude for wave nonlinear growth (Omura et al., 2009). Thus, the solar wind dynamic pressure has a significant impact on the excitation and evolution of chorus waves. In addition, the compressional ULF waves can also modulate chorus waves by changing magnetic field gradient (Li et al., 2022). Simulation results

have clearly shown that the change of the inhomogeneity or curvature of background magnetic field can affect the fine structure of chorus waves (Katoh & Omura, 2013; Kong et al., 2023). Although several studies have reported the appearance and quench of chorus waves caused by the solar wind dynamic pressure (Fu et al., 2012; Liu et al., 2017; Yue et al., 2017; Zhou et al., 2015), there is still no direct observation on the modulation of fine structures of chorus waves by solar wind dynamic pressure.

In this paper, we report the excitation of rising-tone chorus triggered by the sudden increase of solar wind dynamic pressure observed from Van Allen Probes for the first time and demonstrate how the abrupt change of solar wind dynamic pressure affects the fine structure of chorus waves. The paper is organized as follows. We briefly describe the instruments onboard Van Allen Probes in Section 2. The overview and detailed analysis of this event are given in Section 3. Finally, we summarize the principal results and further discuss them in Section 4.

2. Instruments and Data

Van Allen Probes, operating in near-equatorial orbits, were initially put into use in 2012. With a perigee of about 600 km, an apogee of 30500 km, and a flight period of 9 hr, Van Allen Probes provide an unprecedented opportunity for particular studies of the radiation belts due to their high resolution and extensive spatial coverage of orbit. The Electric and Magnetic Field Instrument Suite and Integrated Science (EMFISIS) (Kletzing et al., 2013) onboard Van Allen Probes can provide low-resolution (64 sample/s) magnetic field data, used as the background magnetic field. The complete spectral matrices in the frequency range of 10 Hz–12 kHz from EMFISIS Waveform Receiver (WFR) are used to distinguish chorus waves based on the Singular Value Decomposition (SVD) (Santolík, Parrot, & Lefeuvre, 2003; Santolík, Gurnett, et al., 2003) and the high-cadence (35000 sample/s) magnetic field data are used to analyze the fine structure of chorus waves. The upper hybrid resonance frequency recorded by the EMFISIS High-Frequency Receiver (HFR) is used to obtain the plasma density. The Energetic Particle, Composition, and Thermal Plasma (ECT) suite including the Helium Oxygen Proton Electron (HOPE) and Magnetic Electron Ion Spectrometer (MagEIS) provides the flux and pitch-angle distribution of electrons in different energy channels (Spence et al., 2013). Furthermore, the solar wind dynamic pressure is provided by the OMNI database.

The geomagnetic field model used in this paper is composed of the International Geomagnetic Reference Field (IGRF) and the external field Ts04 (Tsyganenko & Sitnov, 2005). For the sake of accuracy, the geomagnetic field is further corrected by the equation $B_{eq} = B_{loc} \cdot B_{eq,m} / B_{loc,m}$ (B_{loc} is the local measurement; $B_{eq,m}$ and $B_{loc,m}$ are equatorial and local magnetic fields from the Ts04 model; Yu et al., 2018).

3. Observational Results

Figure 1 presents the overview of this event, including the evolution of (a) the plasma density (N_e), (b) solar wind dynamic pressure (P_{dyn}), (c) background magnetic field (B_{obs}), (d) magnetic power spectral densities (B_{psd}), and (e) the angle between the background magnetic field and Poynting vector (θ_{poynt}) from 03:07 to 03:45 UT on 20 December 2015, respectively. The position of Van Allen Probe-B is illustrated by the magnetic latitude (MLAT), magnetic local time (MLT), and L-shell obtained from the Ts04 model at the bottom of Figure 1. During the interval of 03:07 UT to 03:45 UT, the solar wind dynamic pressure increased twice (Figure 1b). The first increase of P_{dyn} started at 03:13 UT and reached the maximum value (~ 11 nPa) at 03:16 UT, with an increase of about 4 nPa. After a slow decline, the second increase of P_{dyn} began at 03:24 UT, increasing from 6.5 nPa to > 15 nPa in about 2 minutes. Accordingly, the intensity of the background magnetic field on the dayside (MLT ~ 12) also enhanced twice with a delay of about 2 minutes (Figure 1c). The enhancements of the background magnetic field are about 25 and 40 nT, respectively, indicating that the solar wind can strongly compress the magnetosphere even at $L = \sim 5.8$ in this event. During the same interval, Van Allen Probe-B detected continuous lower-band chorus waves in the southern hemisphere (Figure 1d), whose magnetic power also correspondingly increased. Besides, an angle of 180° between the background magnetic field and wave Poynting flux indicates that these waves propagated anti-parallel to the background magnetic field, implying the wave was excited at the magnetic equator. Figure 1f shows the minimum cyclotron resonant energies of hot electrons based on the cold plasma dispersion relation and non-relativistic first-order resonance condition. The resonant energy ranges from several to hundreds of keV. For instance, the electron pitch angle distributions for 32, 75, and 101 keV are exhibited in Figures 1g–1i, respectively. During the time interval of 03:07 to 03:45 UT, the flux of these electrons remained high and they had a significant temperature anisotropy. In this case, the enhancement of electron fluxes during the second increase of solar wind pressure should be mainly caused by the substorm injection, which will be discussed later.

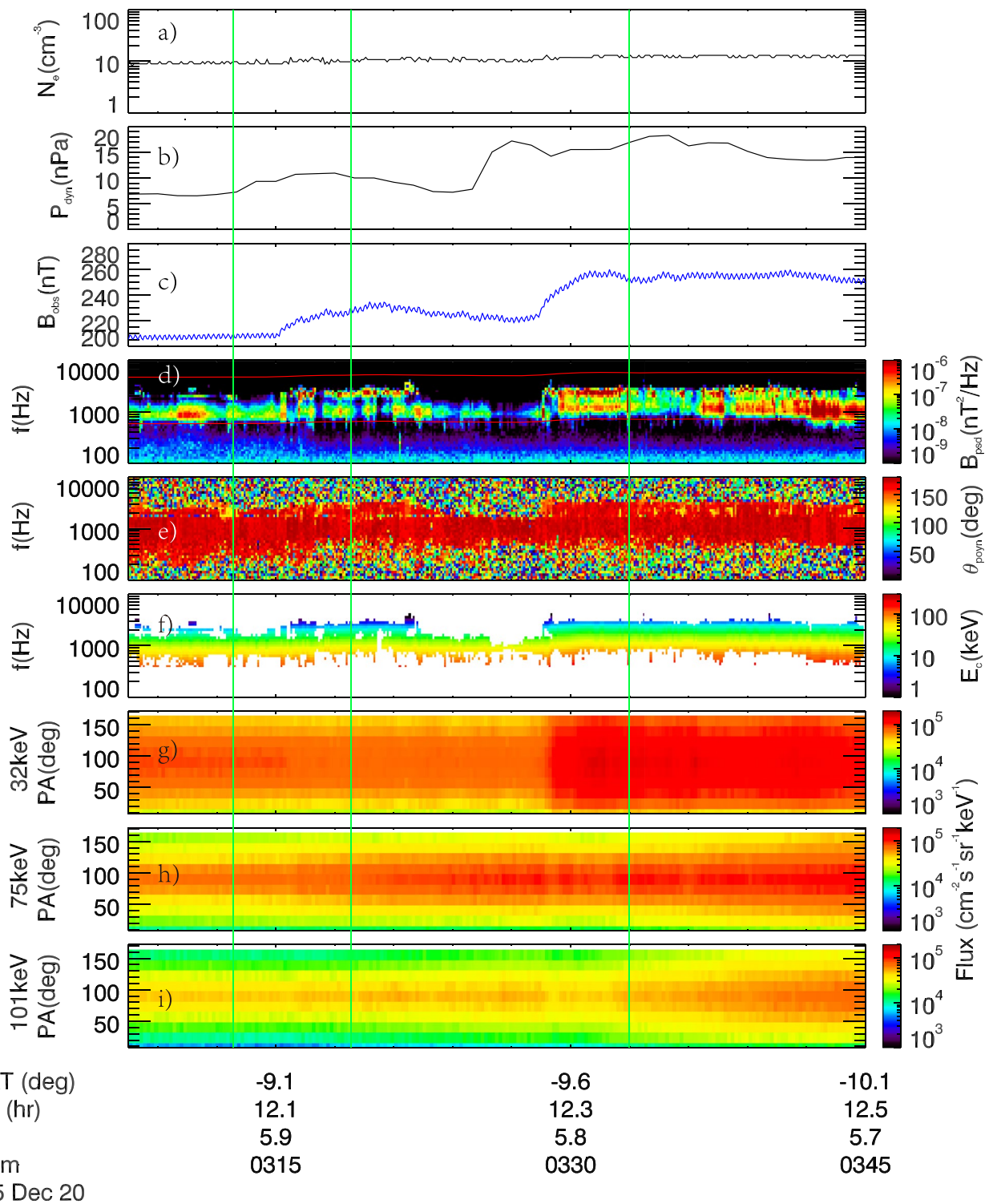


Figure 1. Event overview from 03:07 UT to 03:45 UT on 20 December 2015 recorded by omni-hro 1 min data and Van Allen Probe-B. (a) Plasma density (N_e), (b) solar wind dynamic pressure (P_{dyn}), (c) background magnetic field (B_{obs}), (d) magnetic power spectral densities (B_{psd}), (e) the angle between the background magnetic field and wave pointing flux (θ_{poynt}), (f) the minimum cyclotron resonant energies in the frequency range of chorus waves, (g–i) electron differential fluxes for 32, 75, and 101 keV respectively. The three red lines in (d) represent $0.1 f_{\text{ce}}$, $0.5 f_{\text{ce}}$, and $0.8 f_{\text{ce}}$ respectively.

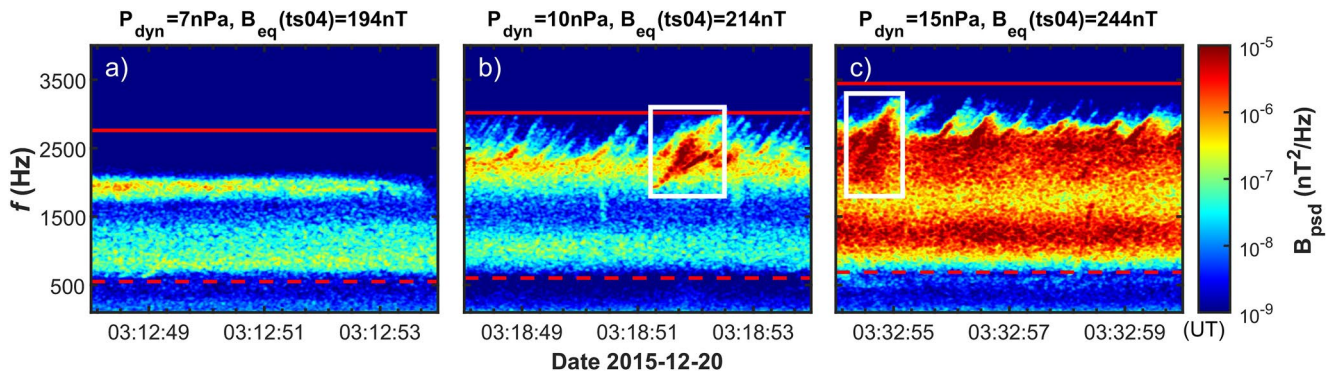


Figure 2. The fine structure of chorus waves before the first increase (03:12:50 UT, a), after the first increase (03:18:50 UT, b), and after the second increase (03:32:58 UT, c) of the solar wind dynamic pressure.

From 03:07 UT to 03:45 UT, there are 130 segments (6 s) of burst-mode waveform data recorded by Van Allen Probe-B WFR, providing excellent support for this study. Figures 2a–2c show the fine structure of chorus waves before the first rise (left), after the first increase (middle), and after the second increase (right) of solar wind dynamic pressure. The selected three intervals (03:12:50, 03:18:50, 03:32:58 UT, and thereafter are referred to as t_1 , t_2 , and t_3) are marked by green lines in Figure 1 and the corresponding magnitude of P_{dyn} and B_{eq} are labeled on the top of Figure 2. The solid red lines and dashed red lines in Figure 2 represent the $0.5 f_{\text{ce}}$ and $0.1 f_{\text{ce}}$ respectively. Before the first rise of P_{dyn} (Figure 2a), chorus waves exhibited the hiss-like structure with a weak amplitude. After the first increase of P_{dyn} (Figure 2b), the rising tones of chorus waves appeared in the higher-frequency band. After the second increase of P_{dyn} (Figure 2c), the chirping rate of rising-tone elements increased and the power density of chorus waves was significantly amplified. However, the structure of chorus waves in the low-frequency band remained unchanged. Such evolution of the fine structure of chorus waves is closely correlated with the two prominent changes of P_{dyn} . For clarity, only three segments of waveform data are demonstrated here, and the burst-mode waveform data over long periods have been examined to ensure the relationship between the variation of P_{dyn} and the fine structures of chorus waves. In addition, Van Allen Probe-A detected similar results to Van Allen Probe-B due to its close position (not shown).

Figures 3a–3c present the observed (circles) and fitted (lines) distributions of electron PSD (phase space density) with energies ranging from tens of eV to hundreds of keV at t_1 , t_2 , and t_3 , respectively. The observations are fitted by a multi-component bi-Maxwellian distribution function:

$$f_M(v_{\parallel}, v_{\perp}) = \sum_j \sqrt{\frac{m}{2T_{\parallel j} \pi}} \frac{m}{2T_{\perp j} \pi} n_j e^{-\frac{mv_{\parallel}^2}{2T_{\parallel j}} - \frac{mv_{\perp}^2}{2T_{\perp j}}}. \quad (1)$$

Since chorus waves are most likely excited at the equator (Figure 1e), then the local distribution parameters have been further projected onto the magnetic equator by Liouville's theorem. The obtained parameters are listed in Table 1. As shown in Figures 3a and 3b and Table 1, the distribution of electron PSD is slightly changed after the increase of P_{dyn} . Figures 3d–3f further illustrate the linear growth rate (blue) near the equator calculated by the linear theory model BO (H. Xie, 2019), and the corresponding amplitudes of chorus waves (black) normalized by background magnetic fields are superposed on it. Before the first increase of P_{dyn} (t_1 , Figure 3d), we find that both the peak and trough of the wave amplitude are consistent with those of the linear growth rate, suggesting the linear excitation of those hiss-like waves. After the first and second rise of P_{dyn} (t_2 and t_3 , Figures 3e and 3f), there are significant inconsistencies between the profiles of wave amplitude and linear growth rate. Combined with the appearance of rising tones, it is reasonable to speculate that the nonlinear effect worked during this period. Moreover, the distribution of electron PSD and the magnitude of linear growth rate stay almost the same before and after the rise of P_{dyn} , indicating that the electron distribution is not the direct cause to trigger the nonlinear effect.

Based on the nonlinear theoretical model proposed by Omura et al. (2008, 2009) and Omura (2021), we further estimate the nonlinear growth rate, threshold amplitude, and optimum amplitude by Equations 2–4:

$$\Gamma_n = \frac{Q\omega_{ph}^2 V_s}{2\gamma U_{\parallel}} \left(\frac{\xi}{\omega\Omega_w} \right)^{1/2} \left(\frac{\chi U_{\perp h}}{\pi c} \right)^{3/2} \exp\left(-\frac{\gamma^2 V_R^2}{2U_{\parallel}^2} \right), \quad (2)$$

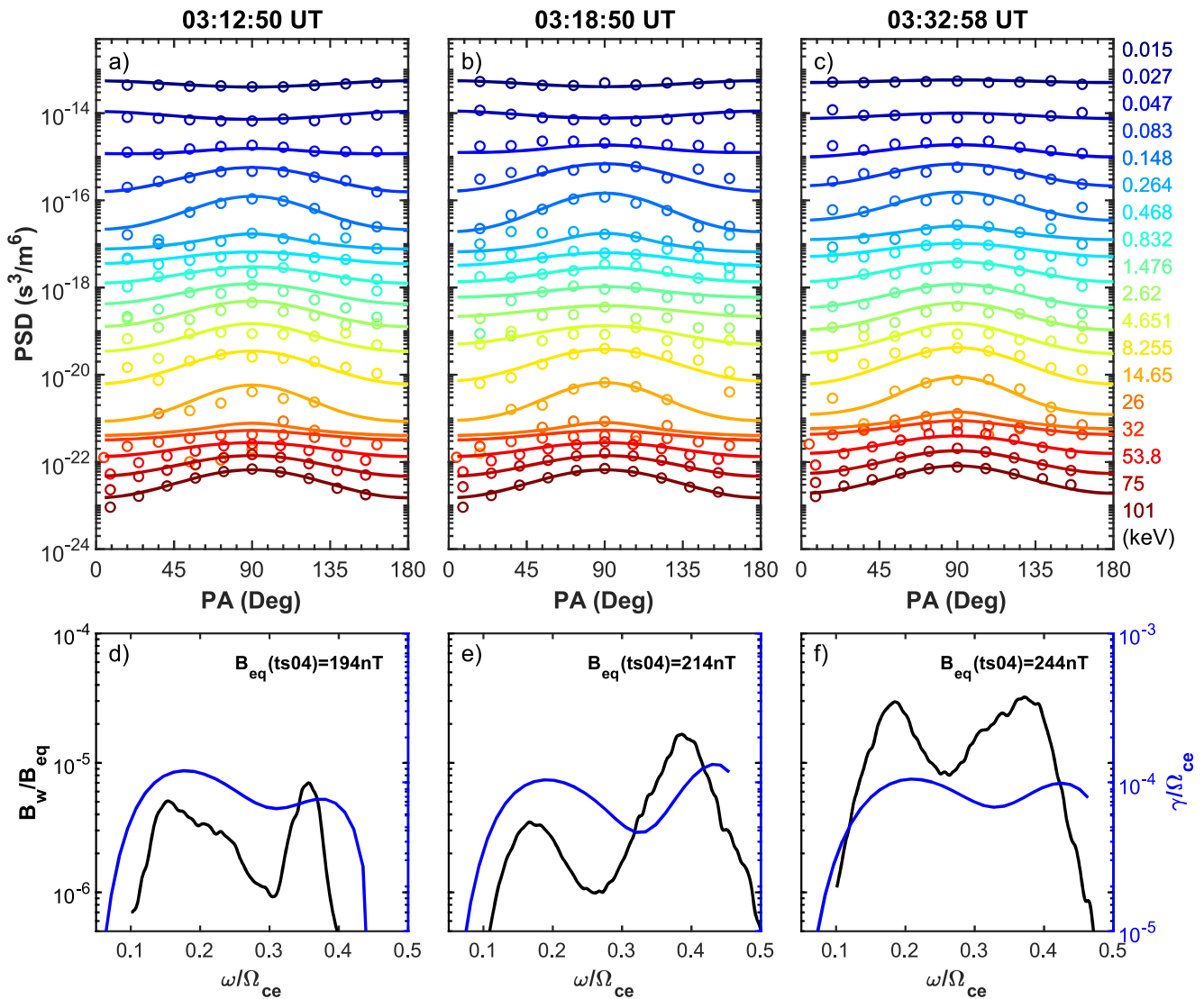


Figure 3. (a–c) Observed (circles) and fitted (lines) electron phase space densities as a function of pitch angle at 03:12:50 (t_1), 03:18:50 (t_2), and 03:32:58 UT (t_3) respectively; (d–f) Linear growth rates (blue) calculated by BO model and the wave amplitudes (black) at the corresponding three moments.

Table 1

Fitting Parameters at 03:12:50 (t_1), 03:18:50 (t_2) and 03:32:58 UT (t_3) Respectively

Component(j)	03:12:50 UT			03:18:50 UT			03:32:58 UT		
	T_{\parallel} (eV)	T_{\perp} (eV)	N (cm^{-3})	T_{\parallel} (eV)	T_{\perp} (eV)	N (cm^{-3})	T_{\parallel} (eV)	T_{\perp} (eV)	N (cm^{-3})
1	7	6	8.22	7	6	8.52	5.7	6	10.8
2	24	42	1.05	23	42	1.26	25	41	1.23
3	200	311	0.104	200	369	0.105	200	306	0.2
4	600	1,288	0.107	900	1,116	0.081	600	1,367	0.084
5	2,000	3,689	0.0632	1,700	3,773	0.075	2,000	4,176	0.063
6	25,000	39,300	0.0083	25,000	39,400	0.0083	15,000	25,700	0.0062

Table 2

Hot Electron Parameters Obtained by Equations 5–7.

	03:12:50 UT	03:18:50 UT	03:32:58 UT
Resonance energy (keV)	5.5–75	3.3–100	4.5–100
N_{he} (cm^{-3})	0.023	0.043	0.039
U_{\parallel}	0.1170 c	0.1040 c	0.1228 c
U_{\perp}	0.2100 c	0.1900 c	0.2212 c

Note. c is for the speed of light.

$$\tilde{\Omega}_{\text{th}} = \frac{100\pi^3\gamma^4\xi}{\tilde{\omega}\tilde{\omega}_{ph}^4(\chi\tilde{U}_{\perp 0})^5} \left(\frac{\tilde{a}s_2\tilde{U}_{\perp}}{Q} \right)^2 \exp\left(\frac{\gamma^2 V_R^2}{U_{\parallel}^2} \right), \quad (3)$$

$$\tilde{\Omega}_{\text{op}} = 0.8\pi^{-5/2} \frac{|Q|\tilde{V}_p\tilde{V}_g\tilde{U}_{\perp 0}}{\tau\tilde{\omega}} \omega_{ph}^2 \left(1 - \frac{\tilde{V}_R}{\tilde{V}_g} \right)^2 \exp\left(-\frac{\gamma^2 V_R^2}{2U_{\parallel}^2} \right). \quad (4)$$

The parameters with a tilde are normalized by background conditions. Here $\xi^2 = \frac{\omega(\omega_e - \omega)}{\omega_{pe}^2}$, $\chi^2 = \frac{1}{1 + \xi^2}$, and $s_2 = \frac{1}{2\xi\chi} \left\{ \frac{\gamma\omega}{\omega_e} \left(\frac{U_{\perp}}{c} \right)^2 - \left[2 + \Lambda \frac{\chi^2(\omega_e - \gamma\omega)}{\omega_e - \omega} \right] \frac{V_p V_R}{c^2} \right\}$.

γ is the Lorentz Factor, c is the speed of light, Λ is equal to 1 for the constant cold electron density model, and ω_{ph} is the plasma frequency of hot electrons. The ratio of the nonlinear transition time to nonlinear trapping period τ is adopted as 2 and 3, and the depth of an electron hole Q is equal to 0.5. The phase velocity V_p , group velocity V_g , and resonance velocity V_R are determined from the cold plasma dispersion. The average perpendicular velocity $U_{\perp 0}$ is equal to $\sqrt{\pi/2} U_{\perp}$. The thermal velocity in the parallel (perpendicular) direction U_{\parallel} (U_{\perp}) and the inhomogeneity factor a are acquired by the following processes.

Assuming that the PSD of hot electrons satisfies the bi-Maxwellian distribution, the characteristic parameters of hot electrons are calculated by Equations 5–7 (Yue et al., 2016):

$$T_{\parallel\text{he}} = \frac{\int_{V_{\min}}^{V_{\max}} V^2 dV \int_0^{\pi} 2\pi \sin \alpha d\alpha m_e V^2 \cos^2 \alpha f(\alpha, v)}{\int_{V_{\min}}^{V_{\max}} V^2 dV \int_0^{\pi} 2\pi \sin \alpha d\alpha f(\alpha, v)}, \quad (5)$$

$$T_{\perp\text{he}} = \frac{\int_{V_{\min}}^{V_{\max}} V^2 dV \int_0^{\pi} 2\pi \sin \alpha d\alpha m_e V^2 \sin^2 \alpha f(\alpha, v)}{\int_{V_{\min}}^{V_{\max}} V^2 dV \int_0^{\pi} 2\pi \sin \alpha d\alpha f(\alpha, v)}, \quad (6)$$

$$N_{\text{he}} = \int_{V_{\min}}^{V_{\max}} V^2 dV \int_0^{\pi} 2\pi \sin \alpha d\alpha f(\alpha, v). \quad (7)$$

According to the frequency range of rising-tone chorus waves, the maximum resonance energy (E_{\max}) and minimum resonance energy (E_{\min}) of hot electrons can be estimated by the cold plasma dispersion relation and non-relativistic first-order resonance condition (Kubota et al., 2018). Furthermore, the distribution of electron PSD $f(\alpha, v)$ has been projected onto the magnetic equator based on Liouville's theorem for accuracy. By integrating above equations, the perpendicular and parallel thermal velocities can be obtained by the formula $U_{\perp} = \sqrt{T_{\perp\text{he}}/m_e}$ and $U_{\parallel} = \sqrt{T_{\parallel\text{he}}/m_e}$. The obtained parameters at 03:12:50, 03:18:50, and 03:32:58 UT are listed in Table 2.

Another important factor featuring in the wave nonlinear growth is the inhomogeneity of the background magnetic field. Smaller inhomogeneity is more conducive to the triggering of rising tones. Figures 4a–4c are the schematic diagram of geomagnetic field configuration at 03:12:50, 03:18:50, and 03:32:58 UT constructed by the International Geomagnetic Reference Field (IGRF) and the external field Ts04. The red cross represents the position of Van Allen Probe-B and the green cross denotes the magnetic equator at the same field line. Comparing Figures 4b and 4c with Figure 4a, we find the dayside geomagnetic field is significantly compressed by the enhanced solar wind dynamic pressure. Figures 4d–4f clearly illustrate the change of the local geomagnetic field along the same field line as a function of the distance (h) from the magnetic equator. By assuming a parabolic geomagnetic field, the inhomogeneity factor a can be acquired by fitting the formula $\Omega_e = \Omega_{e0}(1 + ah^2)$ near the magnetic equator. The fitted values are represented by solid lines in Figures 4d–4f. Based on the relation $\tilde{a} = ac^2/\Omega_{e0}^2$, the normalized inhomogeneity factor \tilde{a} in Equation 3 are 4.9, 3.1, and 1.53, respectively, at the three times. It is clearly shown that the inhomogeneity of the geomagnetic field is significantly reduced by the two increases of the P_{dyn} , which ultimately lead to the excitation of rising tones.

Utilizing the parameters obtained above, the results calculated by Equations 2–4 are shown in Figure 5. The solid (orange and blue) and dashed lines in Figures 5a–5c represent the optimum amplitude and threshold amplitude, respectively. Besides, the amplitude of the selected wave packet (marked in Figure 2) is superimposed on it. At all times, the optimum amplitude never exceeds the threshold amplitude in the low-frequency band of chorus

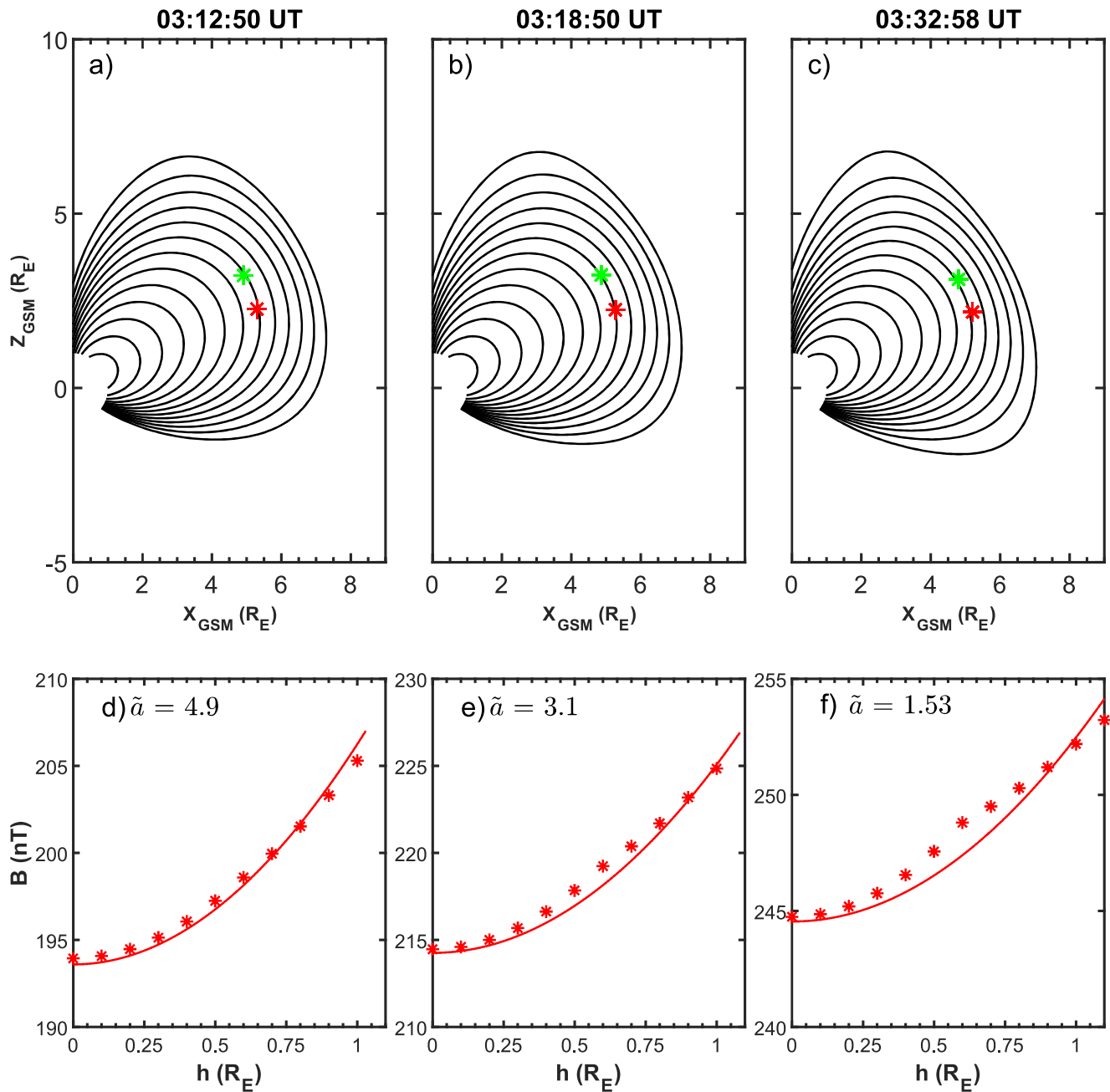


Figure 4. (a–c) The geomagnetic field configuration before the first increase (03:12:50 UT, a), after the first increase (03:18:50 UT, b), and after the second increase (03:32:58 UT, c) of the solar wind dynamic pressure. The red cross represents the location of Van Allen Probe-B and the green cross represents the magnetic equator. (d–f) Local geomagnetic field intensity (circles) and fitted values (lines) along the same field lines as the function of the distance (h) from the magnetic equator at 03:12:50 (d), 03:18:50 (e), and 03:32:58 UT (f) respectively.

waves. Therefore, it is not our focus. Before the rise of P_{dyn} (03:12:50 UT), the threshold amplitude is larger than the optimum amplitude and wave amplitude in the high-frequency band, supporting the absence of nonlinear growth (Figure 5a). After the first increase of P_{dyn} (03:18:50 UT), the threshold amplitude drops significantly, while the optimum amplitude increases. Just as expected, the wave amplitude exceeds the threshold amplitude in the frequency range of higher than $0.37f_{ce}$ (Figure 5b), and the nonlinear process was triggered. However, the wave amplitude remains lower than the optimum amplitude. After the second increase of P_{dyn} (03:32:58 UT), the wave in a wider range of frequencies can satisfy the condition of nonlinear growth (Figure 5c), owing to the further reduction of the threshold amplitude. Now the amplitude of the wave packet reaches the optimum

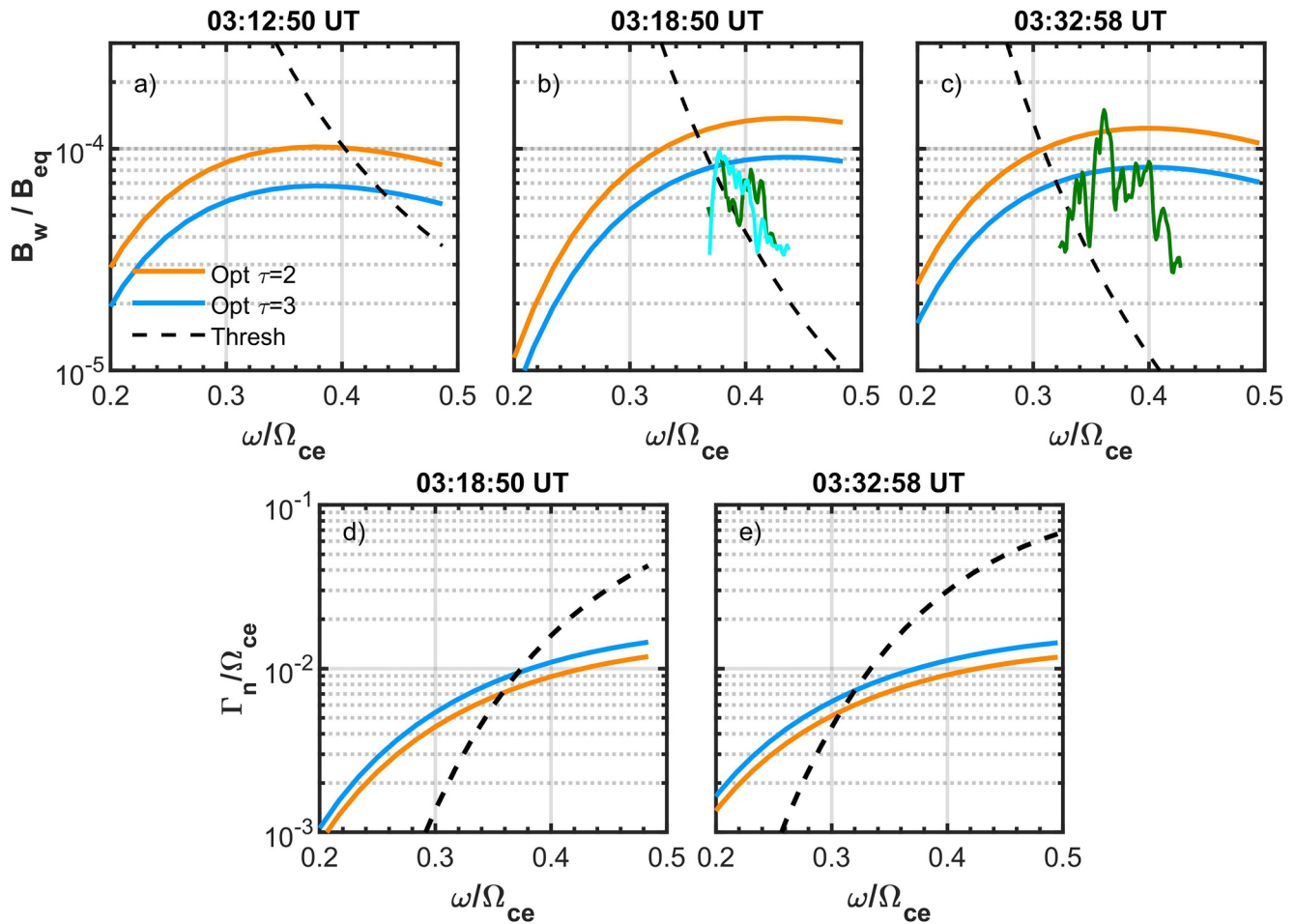


Figure 5. (a–c) Optimal (blue and orange lines) and threshold amplitudes (dashed lines) obtained by Omura’s model at 03:12:50, 03:18:50, and 03:32:58 UT respectively. The selected wave packet amplitudes (marked in Figure 2) are superimposed on it by cyan and green lines. (d–e) Nonlinear growth rates for threshold amplitude (dashed line) and optimum amplitudes (blue and orange lines) at 03:18:50 and 03:32:58 UT respectively.

amplitude. Figures 5d and 5e present the nonlinear growth rates for the threshold amplitude (dashed line) and optimum amplitudes (blue and orange lines) at the last two moments. When the wave amplitude exceeds the threshold amplitude, the wave grows rapidly with the larger nonlinear growth rate (dashed line in Figures 5d and 5e) compared to the linear growth rate (Figures 3e and 3f). Finally, the wave amplitude tends to saturate close to the optimal amplitude (solid lines in Figures 5d and 5e). The nonlinear growth rates for the thresh amplitude and optimal amplitudes are more than two orders of magnitude larger than the linear growth rate, which can explain the clear intensification of chorus waves after the pressure rise.

4. Conclusion and Discussion

In this study, we report the first direct observation of rising-tone chorus triggered by the enhanced solar wind dynamic pressure with Van Allen Probes data. With two sudden increases of the solar wind dynamic pressure, the dayside geomagnetic field is significantly compressed, leading to the reduced inhomogeneity of background magnetic field. Correspondingly, the preexisting hiss-like emissions turn into the clear and intense rising-tone chorus elements. Based on the nonlinear theoretical model, we propose that the nonlinear growth of chorus waves is triggered by the enhanced solar wind dynamic pressure via reducing the inhomogeneity of geomagnetic field as well as the threshold amplitude. This study emphasizes the significance of solar wind dynamic pressure in Earth’s radiation belt dynamics from a micro perspective.

The configuration of dayside magnetic field can be influenced by the solar wind dynamic pressure, which may further affect the electron anisotropy and geomagnetic field inhomogeneity. In some conditions, the electron

betatron acceleration caused by the intensified geomagnetic field can lead to a higher anisotropy, thus providing more free energies to whistler-mode waves (Fu et al., 2012; Jin et al., 2022). However, in another circumstances, the electronic anisotropy does not change significantly, while the variation of magnetic field inhomogeneity modulates the generation and disappearance of chorus waves (Liu et al., 2017; Zhou et al., 2015). However, all of these studies only show the variation of wave intensity modulated by the solar wind dynamic pressure, and there is no direct observation revealing the wave evolution from linear process to nonlinear process. In this paper, we present the evolution of chorus fine structures (from the hiss-like emissions to rising tones) due to the enhanced solar wind dynamic pressure for the first time.

After the first increase of solar wind dynamic pressure, the background electron density and the anisotropy of hot electrons remained nearly unchanged (Tables 1 and 2), suggesting the absence of significant electron betatron acceleration. After the second increase of solar wind dynamic pressure, the electron density increased remarkably ($10.3\text{--}12.24\text{ cm}^{-3}$), while the anisotropy of hot electrons still remained nearly unchanged (Table 2). This suggests that the increase of electron flux should be mainly due to the substorm injection ($AE \approx 500\text{ nT}$ at 03:00 UT) rather than the increase of solar dynamic pressure in this event. However, the inhomogeneity of geomagnetic field is significantly influenced by the two increases of solar wind dynamic pressure. In addition, if we keep the inhomogeneity factor a unchanged after the rise of solar wind dynamic pressure, then the wave amplitude cannot exceed the threshold amplitude and the nonlinear process will not be triggered, supporting the significance of the magnetic field configuration in the formation of rising-tone chorus from the opposite side.

Data Availability Statement

The RBSP data used in this study are available from the website <https://spdf.gsfc.nasa.gov/pub/data/rbsp/>. The omni data are obtained from the website <http://spdf.gsfc.nasa.gov/pub/data/omni/>.

Acknowledgments

This research was funded by the National Key Research and Development Program of China (No. 2022YFA1604600), NSFC Grant (42322406 and 42230201), the Strategic Priority Research Program of Chinese Academy of Sciences Grant (No. XDB41000000), and the “USTC Tang Scholar” program. We also acknowledge the entire Van Allen Probes instrument teams.

References

- Burtis, W. J., & Helliwell, R. A. (1969). Banded chorus-A new type of VLF radiation observed in the magnetosphere by OGO 1 and OGO 3. *Journal of Geophysical Research*, 74(11), 3002–3010. <https://doi.org/10.1029/ja074i011p03002>
- Fu, H. S., Cao, J. B., Mozer, F. S., Lu, H. Y., & Yang, B. (2012). Chorus intensification in response to interplanetary shock. *Journal of Geophysical Research*, 117(A1), A01203. <https://doi.org/10.1029/2011JA016913>
- Gao, X., Chen, L., Li, W., Lu, Q., & Wang, S. (2019). Statistical results of the power gap between lower-band and upper-band chorus waves. *Geophysical Research Letters*, 46(8), 4098–4105. <https://doi.org/10.1029/2019GL082140>
- Gao, X., Chen, R., Lu, Q., Chen, L., Chen, H., & Wang, X. (2022). Observational evidence for the origin of repetitive chorus emissions. *Geophysical Research Letters*, 49(12), e2022GL099000. <https://doi.org/10.1029/2022GL099000>
- Gao, X., Li, W., Thorne, R. M., Bortnik, J., Angelopoulos, V., Lu, Q., et al. (2014). New evidence for generation mechanisms of discrete and hiss-like whistler mode waves. *Geophysical Research Letters*, 41(14), 4805–4811. <https://doi.org/10.1002/2014gl060707>
- Gurnett, D. A., Huff, R. L., Pickett, J. S., Persoon, A. M., Mutel, R. L., Christopher, I. W., et al. (2001). First results from the Cluster wideband plasma wave investigation. *Annales Geophysicae*, 19(10/12), 1259–1272. <https://doi.org/10.5194/angeo-19-1259-2001>
- Horne, R., Thorne, R., Shprits, Y., Meredith, N. P., Glauert, S. A., Smith, A. J., et al. (2005). Wave acceleration of electrons in the Van Allen radiation belts. *Nature*, 437(7056), 227–230. <https://doi.org/10.1038/nature03939>
- Horne, R. B., Glauert, S. A., & Thorne, R. M. (2003). Resonant diffusion of radiation belt electrons by whistler-mode chorus. *Geophysical Research Letters*, 30(9), 1493. <https://doi.org/10.1029/2003GL016963>
- Jin, Y., Liu, N., Su, Z., Zheng, H., Wang, Y., & Wang, S. (2022). Immediate impact of solar wind dynamic pressure pulses on whistler-mode chorus waves in the inner magnetosphere. *Geophysical Research Letters*, 49(5), e2022GL097941. <https://doi.org/10.1029/2022GL097941>
- Katoh, Y., & Omura, Y. (2013). Effect of the background magnetic field inhomogeneity on generation processes of whistler-mode chorus and broadband hiss-like emissions. *Journal of Geophysical Research*, 118(7), 4189–4198. <https://doi.org/10.1002/jgra.50395>
- Kennel, C. (1966). Low-frequency whistler mode. *The Physics of Fluids*, 9(11), 2190–2202. <https://doi.org/10.1063/1.1761588>
- Kletzing, C. A., Kurth, W. S., Acuna, M., MacDowall, R. J., Torbert, R. B., Averkamp, T., et al. (2013). The electric and magnetic field instrument suite and integrated science (EMFISIS) on RBSP. *Space Science Reviews*, 179(1–4), 127–181. <https://doi.org/10.1007/s11214-013-9993-6>
- Kong, Z., Gao, X., Ke, Y., Lu, Q., & Wang, X. (2023). Simulation of chorus wave excitation in the compressed/stretched dipole magnetic field. *Journal of Geophysical Research*, 128(1), e2022JA030779. <https://doi.org/10.1029/2022JA030779>
- Kubota, Y., Omura, Y., Kletzing, C., & Reeves, G. (2018). Generation process of large-amplitude upper-band chorus emissions observed by Van Allen Probes. *Journal of Geophysical Research*, 123(5), 3704–3713. <https://doi.org/10.1029/2017JA024782>
- Li, L., Omura, Y., Zhou, X.-Z., Zong, Q.-G., Rankin, R., Yue, C., & Fu, S.-Y. (2022). Nonlinear wave growth analysis of chorus emissions modulated by ULF waves. *Geophysical Research Letters*, 49(10), e2022GL097978. <https://doi.org/10.1029/2022GL097978>
- Li, W., Mourenas, D., Artemyev, A. V., Bortnik, J., Thorne, R. M., Kletzing, C. A., et al. (2016). Unraveling the excitation mechanisms of highly oblique lower band chorus waves. *Geophysical Research Letters*, 43(17), 8867–8875. <https://doi.org/10.1002/2016GL070386>
- Li, W., Thorne, R. M., Angelopoulos, V., Bortnik, J., Cully, C. M., Ni, B., et al. (2009). Global distribution of whistler-mode chorus waves observed on the THEMIS spacecraft. *Geophysical Research Letters*, 36(9), L09104. <https://doi.org/10.1029/2009GL037595>
- Liu, N., Su, Z., Gao, Z., Zheng, H., Wang, Y., Wang, S., et al. (2017). Simultaneous disappearances of plasmaspheric hiss, exohiss, and chorus waves triggered by a sudden decrease in solar wind dynamic pressure. *Geophysical Research Letters*, 44(1), 52–61. <https://doi.org/10.1002/2016GL071987>

- Lu, Q., Chen, L., Wang, X., Gao, X., Lin, Y., & Wang, S. (2021). Repetitive emissions of rising-tone chorus waves in the inner magnetosphere. *Geophysical Research Letters*, *48*(15), e2021GL094979. <https://doi.org/10.1029/2021GL094979>
- Mourenas, D., Artemyev, A. V., Agapitov, O. V., & Krasnoselskikh, V. (2014). Consequences of geomagnetic activity on energization and loss of radiation belt electrons by oblique chorus waves. *Journal of Geophysical Research*, *119*(4), 2775–2796. <https://doi.org/10.1002/2013JA019674>
- Ni, B., Thorne, R. M., Shprits, Y. Y., & Bortnik, J. (2008). Resonant scattering of plasma sheet electrons by whistler-mode chorus: Contribution to diffuse auroral precipitation. *Geophysical Research Letters*, *35*(11), L11106. <https://doi.org/10.1029/2008GL034032>
- Omura, Y. (2021). Nonlinear wave growth theory of whistler-mode chorus and hiss emissions in the magnetosphere. *Earth Planets and Space*, *73*(1), 95. <https://doi.org/10.1186/s40623-021-01380-w>
- Omura, Y., Hikishima, M., Katoh, Y., Summers, D., & Yagitani, S. (2009). Nonlinear mechanisms of lower-band and upper-band VLF chorus emissions in the magnetosphere. *Journal of Geophysical Research*, *114*(A7), A07217. <https://doi.org/10.1029/2009JA014206>
- Omura, Y., Katoh, Y., & Summers, D. (2008). Theory and simulation of the generation of whistler-mode chorus. *Journal of Geophysical Research*, *113*(A4), A04223. <https://doi.org/10.1029/2007JA012622>
- Omura, Y., & Nunn, D. (2011). Triggering process of whistler mode chorus emissions in the magnetosphere. *Journal of Geophysical Research*, *116*(A5), A05205. <https://doi.org/10.1029/2010JA016280>
- Santolík, O., Gurnett, D. A., Pickett, J. S., Parrot, M., & Cornilleau-Wehrlin, N. (2003). Spatio-temporal structure of storm-time chorus. *Journal of Geophysical Research*, *108*(A7), 1278. <https://doi.org/10.1029/2002JA009791>
- Santolík, O., Parrot, M., & Lefeuvre, F. (2003). Singular value decomposition methods for wave propagation analysis. *Radio Science*, *38*(1), 1010. <https://doi.org/10.1029/2000RS002523>
- Spence, H. E., Reeves, G. D., Baker, D. N., Blake, J. B., Bolton, M., Bourdarie, S., et al. (2013). Science goals and overview of the energetic particle, composition, and thermal plasma (ECT) suite on NASA's Radiation Belt Storm Probes (RBSP) mission. *Space Science Reviews*, *179*(1–4), 311–336. <https://doi.org/10.1007/s11214-013-0007-5>
- Tang, C. L., Li, Z. Y., Angelopoulos, V., Mende, S. B., Glassmeier, K. H., Donovan, E., et al. (2009). THEMIS observations of the near-Earth plasma sheet during a substorm. *Journal of Geophysical Research*, *114*(A9), A09211. <https://doi.org/10.1029/2008JA013729>
- Tsyganenko, N. A., & Sitnov, M. I. (2005). Modeling the dynamics of the inner magnetosphere during strong geomagnetic storms. *Journal of Geophysical Research*, *110*(A3), A03208. <https://doi.org/10.1029/2004JA010798>
- Xie, H. (2019). BO: A unified tool for plasma waves and instabilities analysis. *Computer Physics Communications*, *244*, 343–371. <https://doi.org/10.1016/j.cpc.2019.06.014>
- Yu, J., Li, L. Y., Cui, J., & Wang, J. (2018). Ultrawideband rising-tone chorus waves observed inside the oscillating plasmopause. *Journal of Geophysical Research*, *123*(8), 6670–6678. <https://doi.org/10.1029/2018JA025875>
- Yue, C., An, X., Bortnik, J., Ma, Q., Li, W., Thorne, R. M., et al. (2016). The relationship between the macroscopic state of electrons and the properties of chorus waves observed by the Van Allen Probes. *Geophysical Research Letters*, *43*(15), 7804–7812. <https://doi.org/10.1002/2016GL070084>
- Yue, C., Chen, L., Bortnik, J., Ma, Q., Thorne, R. M., Angelopoulos, V., et al. (2017). The characteristic response of whistler mode waves to interplanetary shocks. *Journal of Geophysical Research: Space Physics*, *122*(10), 10047–10057. <https://doi.org/10.1002/2017JA024574>
- Zhou, C., Li, W., Thorne, R. M., Bortnik, J., Ma, Q., An, X., et al. (2015). Excitation of dayside chorus waves due to magnetic field line compression in response to interplanetary shocks. *Journal of Geophysical Research*, *120*(10), 8327–8338. <https://doi.org/10.1002/2015JA021530>